

^{26}Al in the inner Galaxy

Large-scale spectral characteristics derived with SPI/INTEGRAL

R. Diehl¹, H. Halloin¹, K. Kretschmer¹, A.W.Strong¹, W. Wang¹, P. Jean², G.G. Lichti¹, J. Knödlseeder², J.-P. Roques², S. Schanne³, V. Schönfelder¹, A.von Kienlin¹, G. Weidenspointner², C. Winkler⁴, and C. Wunderer⁵

¹ Max-Planck-Institut für extraterrestrische Physik, D-85741 Garching, Germany

² Centre d'Etude Spatiale des Rayonnements and Université Paul Sabatier, 31028 Toulouse, France

³ DSM/DAPNIA/Service d'Astrophysique, CEA Saclay, 91191 Gif-Sur-Yvette, France

⁴ ESA/ESTEC, Science Operations and Data Systems Division (SCI-SD) 2201 AZ Noordwijk, The Netherlands

⁵ Space Sciences Lab., Berkeley, USA

Received 01 Oct 2005; accepted 17 Nov 2005

Abstract. We performed a spectroscopic study of the 1809 keV gamma-ray line from ^{26}Al decay in the Galaxy using the SPI imaging spectrometer with its high-resolution Ge detector camera on the INTEGRAL observatory. We analyzed observations of the first two mission years, fitting spectra from all 7130 telescope pointings in narrow energy bins to models of instrumental background and the ^{26}Al sky. Instrumental background is estimated from independent tracers of cosmic-ray activation. The shape of the ^{26}Al signal is compared to the instrumental response to extract the width of the celestial line. We detect the ^{26}Al line at $\approx 16\sigma$ significance. The line is broadened only slightly, if at all; we constrain the width to be below 2.8 keV (FWHM, 2σ). The average Doppler velocities of ^{26}Al at the time of its decay in the interstellar medium ($\tau \sim 1.04$ My) therefore are probably around 100 km s^{-1} , in agreement with expectations from Galactic rotation and interstellar turbulence. The flux ($3.3 (\pm 0.4) 10^{-4} \text{ ph cm}^{-2} \text{ s}^{-1} \text{ rad}^{-1}$) and spatial distribution of the emission are found consistent with previous observations. The derived amount of ^{26}Al in the Galaxy is $2.8 (\pm 0.8) M_{\odot}$.

Key words. Nucleosynthesis – Galaxy: abundances – ISM: abundances – Gamma-rays: observations – Methods: observational

1. Introduction

The detailed measurement of 1808.65 keV emission from Galactic ^{26}Al is one of the design goals of the INTEGRAL mission (Winkler et al. 2003). ^{26}Al gamma-rays were discovered in 1982 by HEAO-C (Mahoney et al. 1982), and since then have been considered to be direct proof of ongoing nucleosynthesis in the Galaxy. From the 9-year mission of the Compton Gamma-Ray Observatory, in particular from the COMPTEL imaging Compton telescope, all-sky imaging in the 1.8 MeV gamma-ray line from ^{26}Al had been obtained (Diehl et al. 1995; Oberlack 1997; Knödlseeder et al. 1999; Plüschke et al. 2001). From these measurements, we learn that ^{26}Al emission extends all along the plane of the Galaxy; hence ^{26}Al nucleosynthesis is a common Galactic phenomenon rather than local to the solar system. The irregular structure of the emission, alignments of emission maxima with spiral-arm tangent, and comparisons with tracers of candidate ^{26}Al sources all have pointed to the conclusion that massive stars dominate ^{26}Al

nucleosynthesis (Chen et al. 1995; Prantzos and Diehl 1996; Knödlseeder et al. 1999; Knödlseeder 1999).

The high spectral resolution of Ge detectors of 3 keV (FWHM) at the ^{26}Al line energy of 1808.65 keV is expected to reveal more information about the sources and their location through Doppler broadenings and shifts, induced from Galactic rotation and from dynamics of the ejected ^{26}Al as it propagates in the interstellar medium around the sources. This should add important new astrophysical perspectives, beyond what could be learned from the large imaging database of the COMPTEL sky survey.

Significant broadening of the ^{26}Al line has been found by the GRIS team from its Ge detector instrument through a balloon experiment (Naya et al. 1996). The reported intrinsic ^{26}Al line width of 5.4 keV corresponds to velocities above 450 km s^{-1} for decaying ^{26}Al isotopes, if interpreted dynamically, from Doppler shifts. Various attempts were undertaken to understand how such high velocities could be maintained on time scales of Myrs (Chen et al. 1997; Sturmer & Naya 1999). It was clear that only rather unusual circumstances such as large interstellar cavities, or high fraction of ^{26}Al being deposited onto grains near the ^{26}Al sources, could offer an expla-

Send offprint requests to: R. Diehl
Correspondence to: rod@mpe.mpg.de

nation. With recent space-based gamma-ray spectroscopy experiments, in particular from the RHESSI (Lin et al. 2002) and INTEGRAL (Winkler et al. 2003) missions, it became apparent that the GRIS result may not be valid (Smith 2003, 2004; Diehl et al. 2003, 2004). The interstellar medium surrounding sources of ^{26}Al may be less extreme; ^{26}Al is considered an important probe of these astrophysical sites.

In this paper, we discuss our analysis of data from the SPI spectrometer on INTEGRAL with respect to the intrinsic ^{26}Al line width and to the large-scale properties of ^{26}Al emission in the inner Galaxy, exploiting data from the first two years of the mission.

2. Observations, data and analysis

2.1. Data selections and standard processing

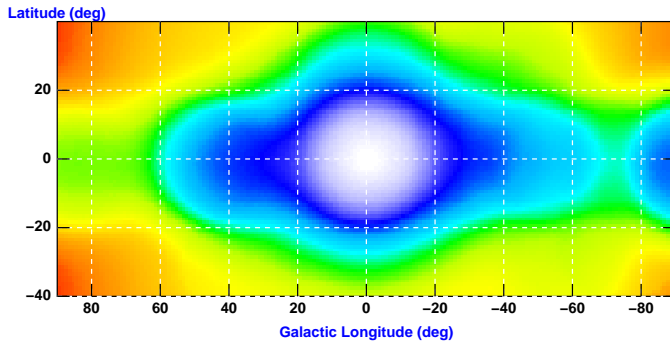


Fig. 1. Exposure of the inner Galaxy for the data as selected from orbits 15-259 for our study. At the Galactic center, the effective exposure is 4 Ms, at longitudes $\pm 50^\circ$ 0.85 Ms (linear scale).

We analyze data from the SPI instrument, the coded-mask imaging spectrometer instrument on INTEGRAL, with its 19-element Ge gamma-ray camera; the SPI instrument and its performance are described in (Vedrenne et al. 2003; Roques et al. 2003). For the results reported here, we use data from the INTEGRAL Core Program (which focuses on a survey of the inner Galaxy), our Open Program data, and data that were publicly available at the time of this analysis. Our database spans INTEGRAL orbits 15–259, and our filtering to obtain data free from contamination due to increased-background events or other anomalies yields a total observing time of 16.5 Ms from this set. Filtering the data of glitches towards the perigee near the radiation belts of the Earth, from solar-flare periods, and from otherwise anomalous background conditions was essential in order to obtain a sufficiently homogeneous database in terms of background handling. We selected data within orbit phases 0.1–0.9 in order to exclude orbital phases near the Earth’s radiation belts, we excluded data where the saturated Ge count rate exceeds 10^5 counts s^{-1} to reject anomalies, and we excluded solar-flare periods with a 1-day window triggered by the >30 MeV count rate of the GOES proton monitor exceeding a value of 0.5 Hz.

Our standard processing includes calibration of the energy scale once per orbit by fitting Gaussians to strong instrumental lines. This attains a relative precision of 0.05 keV at 1809 keV over these 1.5 years of data (Lonjou et al. 2004). The non-symmetric line profiles, which develop from degradation of the Ge detectors due to cosmic-ray bombardement, result in shifts of the energy scale of a few tenths of keV at 1809 keV. Due to calibration-line fitting with symmetric Gaussians, these detector degradations mainly result in slight broadenings of the effective instrumental line resolution; the offset in the absolute energy scale should be below 0.1 keV. For each pointing of the instrument, standard processing assembles the energy spectra of each of the Ge detectors at 0.5 keV binning, together with detector deadtimes and various housekeeping data used for data selections and for background modelling.

In this study, we make use of single-detector hits only, leaving coincident hits of more than one detector aside. Although this reduces the overall detection efficiency by about 50 %, our background and spectral-response modeling is substantially more straightforward for this case. Altogether our database covers the Galactic plane (pointings within 30 degrees latitude) with 7130 pointings (135470 spectra), equivalent to a total deadtime-corrected exposure of 12.86 Ms, with, e.g., 4 Ms at the Galactic center and 0.85 Ms at longitudes $\pm 50^\circ$ (see Fig. 1).

2.2. Background treatment

Typically, source signals such as Galactic ^{26}Al contribute only at the percent level, the remainder of the total signal being instrumental background. Therefore the treatment of background is a key aspect of the achieved sensitivity and suppression of systematics, as is the case for all gamma-ray instruments. In principle, with SPI and its coded mask we can distinguish “signal” from “background” by comparing the 19-detector amplitude patterns $r_j = d_j / \sum_j d_j$ between sky observations and a suitable reference (j is detector index, d is counts); instrumental background should be responsible for a pattern independent of instrument pointings. But diffuse sky emission such as from Galactic ^{26}Al is modulated rather weakly by the coded mask between successive pointings with typically 2° offsets, unlike for strong point sources. Therefore, the “background reference” pattern cannot be taken from pointings nearby in observing time, which is desirable to probe a similar background situation. For our large database, however, which spans a considerable range in time and sky-pointing directions, we can detect the celestial diffuse ^{26}Al signal when we use the time-averaged data for the background pattern reference (see Fig. 3). Independent data are preferable, e.g. when the instrument was pointed towards high latitudes, or using detector count rates outside the energy range of interest, or using independent tracers of instrumental background. Instrumental-background differences between such references and actual data may be expected, though; some time variation in the background model should be allowed for by using additional parameters when fitting measurements.

Following this general idea, we developed a background model for our study; more details will be described in a forth-

coming paper (Halloin et al., in preparation). We base our model on presumed tracers of instrumental background, and optimize these to then establish the “background” detector ratio pattern per pointing.

First, we correlate a larger set of potential background tracers with the count-rate variations in our energy band of interest around the ^{26}Al line. We choose the broad band of 1800–1820 keV for this correlation, and the mission part where all 19 detectors of the camera were fully functional. We sum over all 19 detectors to improve statistical precision for the detector data. This allows us to identify correlations of candidate background tracers with actual background variations in our camera with high significance. The best-correlated tracer is identified as the “prime” background tracer. Then we remove the information of this prime tracer from all other candidate tracers through orthogonalization, and again correlate the (now additional to our prime tracer, or orthogonal-only) components of the other candidate tracers with our count rates, to iteratively find more “next-best” tracers. No more than three orthogonalized background-tracer components are needed for adequate background modelling of the energy bands around the ^{26}Al line. This first step allows us to identify the necessary set of tracers and their decomposition order. We find a hierarchy of (1) non-saturated Ge camera count rate, (2) cumulative saturated Ge counts since mission start, and (3) plastic anticoincidence count rate. In a second step, this decomposition scheme is applied to our spectroscopic dataset in 0.5 keV energy bins, separately for three time ranges to account for the two detector failures. This determines for each tracer template the detector patterns of instrumental background as fitted to the measured data. In this way, our background model is based on actual background-tracer data with their high statistical precision and high time resolution, yet the detector count ratios within the 19/18/17-element camera and per energy bin may be different. In the final model fitting step (see next Section 2.3), only a few (3–10) background parameters are adjusted to allow for gradual drifts of signal-to-background ratios with time, and/or to account for normalization differences for the times where one or two detector elements of our camera (detectors 2 and 17) failed.

2.3. Spectra determination

Our measured data consist of spectra per detector and pointing (the typical spectral signatures are illustrated in the cumulative spectrum shown in Fig. 2). We derive our spectra of celestial emission by fitting our set of model components for background and a (set of) model (components) for the spatial distribution of celestial emission to our data, fitting amplitude coefficients independently for fine energy bins in the range 1800–1820 keV (see also Strong et al. 2005, for method details). The count data in our spectra per pointing and detector are modelled as:

$$d_{ijk} = \sum_{m,n}^{N_S} R_{ijk}^{mn} \sum_s \Theta_s S_s^{mn} + \sum_t \sum_b^{N_B} \Theta_{b,t} B_{b:ijk}$$

with i,j,k as indices for data space dimensions *energy*, *detector*, *pointing*, m,n indices for sky dimensions *longitude*, *latitude*,

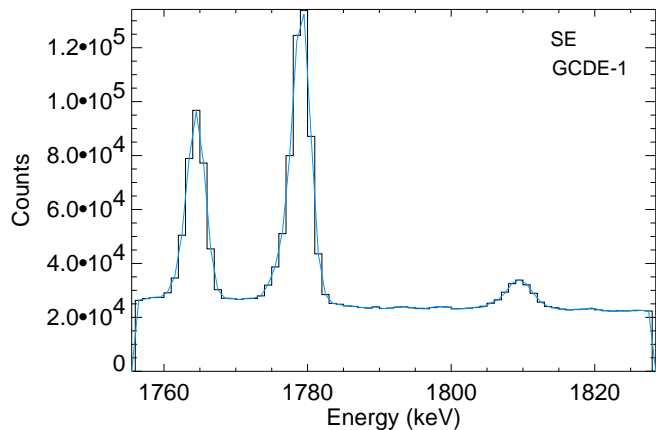


Fig. 2. Raw data spectrum in the region around the ^{26}Al line, illustrating instrumental line and continuum backgrounds (from single-detector events (SE) during the first inner-Galaxy survey (GCDE-1)). Line origins are radioactivities excited by cosmic ray bombardements, specifically ^{205}Bi (1764.3 keV), ^{28}Al (1779.0 keV), and ^{26}Na (1808.7 keV) with ^{26}Mn (1810.9 keV) for the composite feature underlying the ^{26}Al line (Weidenspointner et al. 2003). Fitting these instrumental lines we typically find centroids and widths of (1764.4/3.1), (1779.0/3.2), and (1809.4/4.2), respectively. The intensity of the instrumental feature at 1809.4 keV is typically 12% of the instrumental line at 1779 keV.

and N_S sky model components S , N_B background model components B . The skymaps S are convolved into the data space of measured spectra for each detector using observation attitude information and the instrumental response, which had been determined from Monte Carlo simulations and was adjusted to prelaunch calibration measurements (Sturmer et al. 2003). We assess the quality of the fit through checks on its global precision (χ^2) and on the residuals of the fit to our 135470 measured spectra. Typical χ^2 values per degree-of-freedom range from 1.5 in the instrumental background line at 1779 keV to 0.8–1.2 in the ^{26}Al line region. Typical statistical errors in fitted flux values per bin are $0.12 \text{ ph cm}^{-2} \text{ s}^{-1} \text{ rad}^{-1} \text{ keV}^{-1}$. Systematic uncertainties can be estimated by increasing errors per data point until the fit quality criterion χ^2 yields a value of 1.0; we derive systematic uncertainty to be 40% of the value for statistical uncertainties. Coefficients Θ for the background intensity (time variation allowed) and for the skymap intensity (constant in time) are derived, the latter (Θ_s) comprising the resultant spectrum of the signal from the sky (e.g. Fig. 3).

The celestial origin of the observed feature near 1809 keV has been verified through identical analysis on a dataset from high-latitude observations (Fig. 3), where the signal disappears. Moreover, the instrumental feature at 1810 keV (see Fig. 2, leaking also into the high-latitude data spectrum in Fig. 3 (top)) is clearly offset from the observed signal, and is significantly broader, due to its origin as a composite of local radioactivities (Weidenspointner et al. 2003).

The instrumental line-shape variation due to degradation of detectors was determined during the mission by fitting a spe-

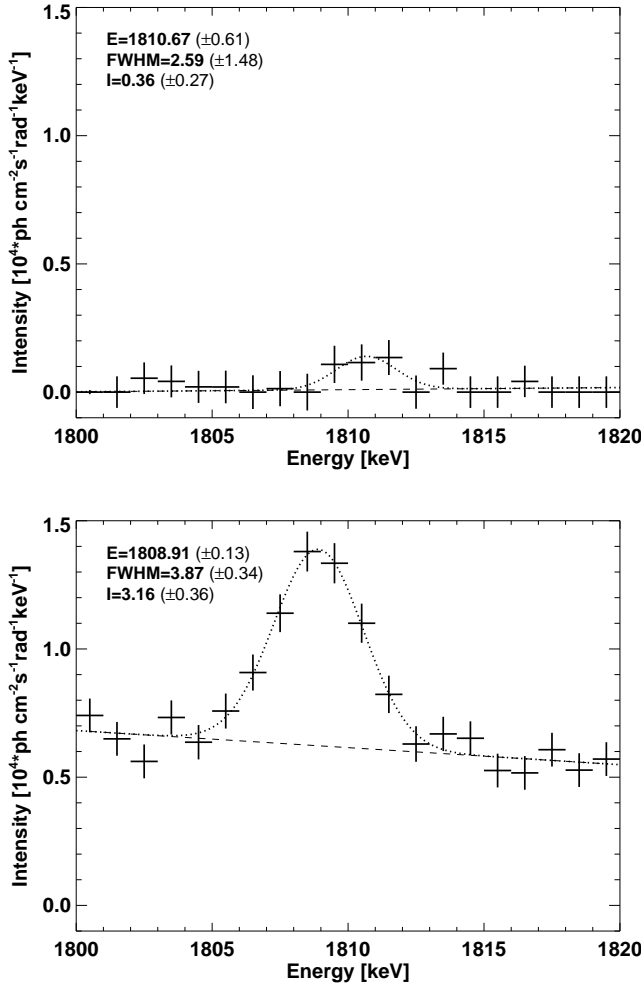


Fig. 3. Test for spurious instrumental background leakage into spectra for celestial emission: Sky model fitting was applied to high-latitude data (above), and to data from the inner Galaxy (below). The sky intensity distribution was modeled from the COMPTEL ^{26}Al skymap, and the pointing pattern of the inner Galaxy was adopted also for the high-latitude data. As a simple background model we use globally-averaged data; this background model still correlates with the measurements as taken along the Galactic plane, which causes non-zero intensities at all energies. Nevertheless, the celestial ^{26}Al line is revealed from the increased correlation with the skymap around 1809 keV for the Galactic-plane data.

cific spectral response to instrumental lines which captures a degradation parameter τ (see Fig. 4). This spectral response function consists of a Gaussian shape which characterizes each particular detector’s intrinsic resolution, and a one-sided exponential function extending from the peak of the Gaussian towards lower energies, which characterizes the pulse height losses due to detector degradation through its width τ :

$$s_i = s_0 \cdot \int_0^{\infty} \left(\frac{1}{\sqrt{2\pi}\sigma} \cdot e^{-\frac{(E_i+E'-E_0)^2}{2\sigma^2}} \cdot \frac{1}{\tau} e^{-\frac{E'}{\tau}} \right) dE'$$

with s_i the amplitude per energy bin E_i , E_0 the photopeak line energy, and σ the instrumental resolution of the Ge detector.

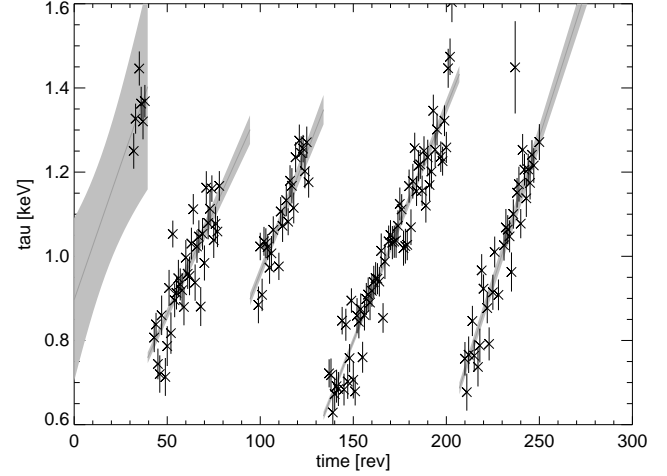


Fig. 4. Evolution of the detector resolution with time for the region around 1800 keV. The width τ of the one-sided exponential which we use to describe degradation, averaged over all 19 detectors, evolves with time (expressed here in 3-day intervals of the satellite orbits) due to degradation and detector annealings. The grey areas represent the linear approximations which we adopted for modelling detector degradations, with their uncertainties (Kretschmer et al., in preparation).

By fitting many calibration lines over the SPI energy range, the time-variable degradation has been determined (see Fig. 4). In this analysis, we use this spectral-response behaviour to accumulate the expected instrumental line shape, which we use in fitting the celestial signal in our ^{26}Al line spectra and to derive constraints on the additional broadening caused by intrinsic velocity variances of decaying ^{26}Al (e.g. Fig. 6, see below). We plan to take this time-variable spectral response directly into account in our instrumental response when convolving the input sky, and then also by our modeling of instrumental features of the background (Kretschmer et al., in preparation).

In fitting non-analytical spectral shapes to our spectra, such as our time-integrated instrumental-response line shape convolved with intrinsically-broadened ^{26}Al emission, gradient-driven fit algorithms are inadequate - in particular when we aim to determine a parameter like the intrinsic ^{26}Al width, which is convolved with the instrumental line profile before being compared to our flux values per energy bin. The probability distribution in this case is very asymmetric, but we wish to perform quantitative statistical analysis of our findings. This is not possible with tools that inherently assume symmetric and smooth probability distributions for parameter fluctuations. We make use of the Monte Carlo Markov Chain method, preprocessed by simulated annealing (Metropolis et al. 1953; Neal 1993). This method migrates through the plausible parameter space as guided by prior knowledge about the parameters, but in a random-walk like fashion; for large numbers of samples, this assembles the parameter value probability distributions rather well also for less idealized cases (see Fig. 6 and next Section), allowing us to derive an upper limit for the intrinsic ^{26}Al line

width. Varying priors within plausible ranges has an insignificant impact on our obtained numerical value.

3. Results

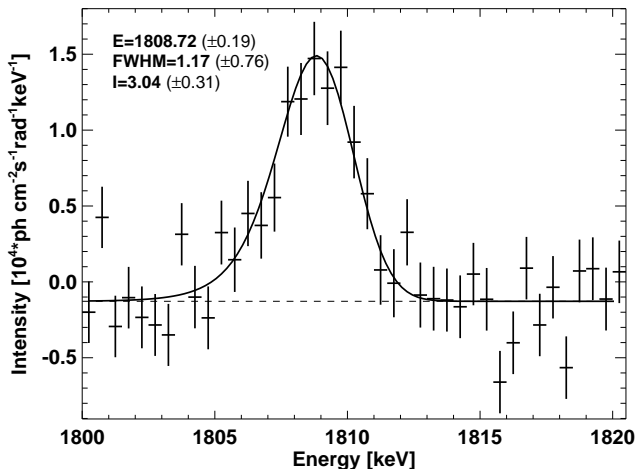


Fig. 5. Spectrum derived from sky model fitting using COMPTEL ^{26}Al MaxEnt image and the “orthogonalized tracers” background model. The fit (solid line) uses the shape of the instrumental resolution as it results from cosmic-ray degradation and annealings during the time of our measurement (see Fig. 4), convolved with a Gaussian for the intrinsic ^{26}Al width, as fitted by MCMC. The ^{26}Al line width constraints are highly asymmetric (see Fig. 6). Intensities are quoted in units of $10^{-4} \text{ ph cm}^{-2} \text{ s}^{-1} \text{ rad}^{-1} \text{ keV}^{-1}$.

By fitting our set of observations at 0.5 keV wide energy binning with the sky intensity distribution of ^{26}Al as imaged by COMPTEL together with our background model based on orthogonalized background tracers, we obtain the spectrum for ^{26}Al emission from the inner Galaxy shown in Fig. 5. The ^{26}Al line is detected at 16σ significance. The line component above the linear component of our spectral fit determines the intensity of observed ^{26}Al . The total ^{26}Al gamma-ray flux as determined for the inner Galaxy region ($-30^\circ < l < 30^\circ$ and $-10^\circ < b < 10^\circ$, i.e. the flux in the inner radian) obtained from this fit is $3.3 (\pm 0.4) 10^{-4} \text{ ph cm}^{-2} \text{ s}^{-1} \text{ rad}^{-1}$. This is consistent with both the value of about $4 10^{-4} \text{ ph cm}^{-2} \text{ s}^{-1} \text{ rad}^{-1}$ concluded from previous measurements (Prantzos and Diehl 1996) and in particular the COMPTEL imaging-analysis value of $2.8 (\pm 0.4) 10^{-4} \text{ ph cm}^{-2} \text{ s}^{-1} \text{ rad}^{-1}$ (Plüschke 2001; Oberlack 1997). When we vary the model sky among plausible models, we obtain slightly different flux values, within expectations for the respective candidate ^{26}Al source maps. The variance of flux values in our sample (see Table 1 and Diehl et al. (2005)) is $1.2 10^{-5} \text{ ph cm}^{-2} \text{ s}^{-1} \text{ rad}^{-1}$ or 4%; we adopt this as our systematic flux uncertainty.

The detection of the celestial ^{26}Al line is significant ($> 3\sigma$) in 6 of the 0.5 keV-wide bins covering the ^{26}Al line; this allows us to derive line shape details for the ^{26}Al line.

Table 1. ^{26}Al line results for different sky distribution models

Sky Model	$d\lambda^1$	I^2	dI^2	width ³
exponential disk ⁴	n/a	2.88	0.33	1.09
young disk ⁵	-0.62	3.22	0.43	1.19
free electrons ⁶	-1.49	3.54	0.36	1.05
Ne2001(180) ⁷	-2.87	3.22	0.38	1.34
Ne2001(140) ⁸	-2.22	3.06	0.41	1.22
dust $100\mu\text{m}$ ⁹	-1.14	4.01	0.42	1.17
COMPTEL ^{26}Al ¹⁰	-0.70	3.04	0.31	1.17

¹ Fit quality: likelihood ratio difference to first model

² in units of $10^{-4} \text{ ph cm}^{-2} \text{ s}^{-1} \text{ rad}^{-1}$

³ mean of celestial line width (see Fig.6)

⁴ exponential disk, scale radius 4 kpc, scale height 180 pc

⁵ young disk from Robin et al. (2003), scale height 125 pc

⁶ free electron spiral arm model from pulsar dispersion measurements (Taylor & Cordes 1993), scale height 180 pc

⁷ free electron model from Cordes & Lazio (2002), no thick disk, scale height 180 pc

⁸ as ⁷, but scale height 140 pc

⁹ IRAS $100 \mu\text{m}$, from *skyview* (Wheelock et al. 1991), after subtraction of Zodiacal light

¹⁰ ME map from Plüschke et al. (2001)

First, the line centroid is determined at $1808.72 (\pm 0.19(\text{stat}) \pm 0.1(\text{syst})) \text{ keV}$ from fitting our model shape to the observed feature (see above). This is well within the laboratory value for the ^{26}Al line of $1808.65 (7) \text{ keV}$ (Firestone and Ekström 2004). The variance of line centroids for the different models of Table 1 is 0.002 keV .

Second, the ^{26}Al line shape rather closely resembles the one expected from instrument properties such as intrinsic resolution and degradations as experienced between annealings. We fit the effective accumulated instrumental line shape, convolved with a Gaussian for the celestial ^{26}Al line broadening, to our spectrum. The fitted parameters are the line centroid, the intrinsic width of celestial ^{26}Al , the intensity of the line, and two parameters for the underlying continuum. The intrinsic line width appears to be rather small. But this parameter is not as “well-behaved” as the others: The parameter probability distribution should be symmetric as for a Gaussian, its width then reflects the uncertainty of the fitted parameter value. The probability distribution for the ^{26}Al line width, however, peaks at small values near 0.2 keV , with a minor reduction towards zero intrinsic line width, and gradually decreases towards larger line widths (Fig. 6). Formal determination of the mean of this probability distribution (to yield a “fitted width value”) and its width (to yield the “width uncertainty”) is not appropriate. (Nevertheless, we show these results in spectra Figures to at least coarsely describe the intrinsic line broadening). Therefore, we obtain the probability distribution from the Monte Carlo Markov Chain parameter fitting; we integrate this distribution over the desired probability fractions to obtain upper limits for the intrinsic ^{26}Al line width, see Fig. 6: For a 95% probability equivalent to a “ 2σ ” limit, we thus obtain a limit of 2.8 keV from our SPI measurement, while the GRIS value of 5.4 keV has a probability of $3 10^{-5}$. It turns out that the spectral details (line position and width) are practically identical for different adopted sky

distributions, while ^{26}Al flux values vary by about 4% among different plausible models (Diehl et al. 2005).

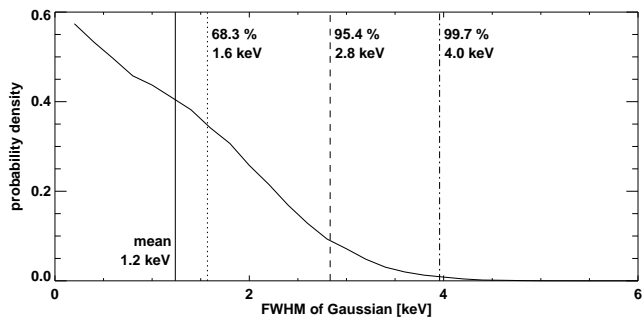


Fig. 6. Probability distribution for the ^{26}Al intrinsic line width as fitted in Fig. 5. The formal results (Fig. 5) derived from the mean and width of this distribution are inadequate descriptions of this highly asymmetric probability distribution. Rather, an upper limit of 2.8 keV (2σ) applies, and an intrinsically even much narrower line is fully consistent with our measurement.

4. Discussion

Our new measurement of the inner-Galaxy integrated ^{26}Al emission yields a flux that translates into a Galactic steady-state mass of $2.8 (\pm 0.8) M_{\odot}$ (see Diehl et al. 2005, for details and implications). From a comparison to earlier measurements (see Prantzos and Diehl 1996), our flux value is on the low side of the average among experiments. This trend for imaging versus large field-of-view experiments may suggest that either imaging helps to suppress instrumental background leakage, or that there is some large-scale extended ^{26}Al emission from nearby sources.

As a first step towards spatially resolved spectroscopy, we separately determined spectra for the inner region of the Galaxy ($-40^{\circ} < l < 40^{\circ}$, $-10^{\circ} < b < 10^{\circ}$) using a smooth exponential-disk model with scaling parameters 4 kpc (radius) and 180 pc (latitude extent), which we split into three longitude segments at -10° and 10° . This obtains spectra for the different segments (Diehl et al. 2005, and references therein). Fitting the ^{26}Al line as above, we obtained differences in line centroids compatible with expectations from Galactic rotation: the ^{26}Al line is slightly blue-shifted at negative longitudes and red-shifted at positive longitudes. This supports the view that the observed ^{26}Al emission arises from the inner Galaxy region, rather than foreground. This reaffirms the above Galaxy-wide steady-state interpretation of the measured ^{26}Al flux and determination of the total ^{26}Al mass in the Galaxy (Diehl et al. 2005). Furthermore, these spatially separated spectra also support the asymmetry of the ^{26}Al emission in the inner Galaxy indicated in COMPTEL images (Plüschke et al. 2001), in that the 4th quadrant appears brighter than the 1st.

It is evident that line broadenings of a few keV disagree with our data from the inner Galaxy (Figs. 5 and 6); thus, velocities of decaying ^{26}Al isotopes are modest. The GRIS measurement of 5.4 keV line broadening appears inconsistent with

all other measurements to date and is clearly ruled out by our result.

A line broadening of 0.8 keV corresponds to thermal Doppler velocities of 100 km s^{-1} , as a reference. In the inner Galaxy, Galactic rotation alone leads to Doppler shifts, which are particularly pronounced towards longitudes $\pm 30^{\circ}$, and range up to 0.25 keV (Kretschmer et al. 2003); a line broadening of about 1 keV had been estimated if integrated over this inner region of the Galaxy (Kretschmer et al. 2003). Are our line-shape constraints consistent with Galactic-rotation effects and standard interstellar velocities?

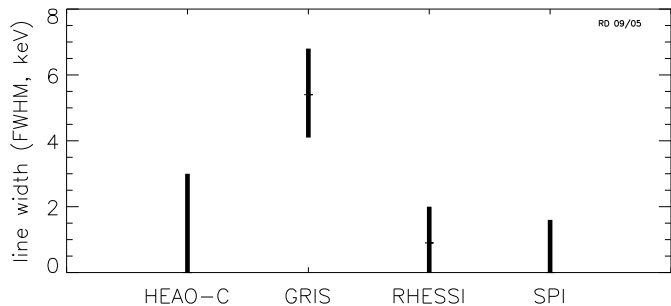


Fig. 7. Constraints on the width of the ^{26}Al line from different instruments (1σ error bars).

We believe so (Diehl et al. 2005), and consider the measured line width of ^{26}Al from the inner Galaxy to be consistent with Galactic rotation and modest (see below) interstellar-medium turbulence around the sources of ^{26}Al . We thus confirm earlier results obtained by HEAO-C, RHESSI, and SPI on INTEGRAL (Mahoney et al. 1982; Smith 2003; Diehl et al. 2004) (see Fig. 7). This is reassuring: neither the suppression of deceleration of ^{26}Al before decay in large, kpc-sized cavities around its sources nor other exotic explanations (Chen et al. 1997) are required to account for a large broadening of the ^{26}Al line.

How much line broadening from ISM is plausible? Some broadening is expected from the apparent existence of major interstellar cavities in the regions of massive-star clusters (Oey 1996), and from the ejection kinematics of these presumed ^{26}Al sources, i.e. winds and supernovae. WR wind velocities are 1200 km s^{-1} (Vink & deKoter 2005) or higher (Plüschke 2001), and models for ejection of ^{26}Al by core-collapse supernovae predict velocities in the same range (Herant & Woosley 1994). Therefore it will be interesting to test with SPI on INTEGRAL whether we can observe such effects for localized regions of ^{26}Al emission. Here sources may not yet have obtained a long-term equilibrium with their surrounding ISM, and ^{26}Al may thus be preferentially decaying from its initial and fast phase, rather than already being slowed down to normal ISM velocities in the 10 km s^{-1} range. The first SPI results of a modestly-broadened ^{26}Al line in the Cygnus region (Knödseder et al. 2004), as well as the COMPTEL result of the Orion region (where ^{26}Al emission appears offset from its sources in the Orion OB1 association towards the Eridanus cavity (Diehl 2002)), are hints that ^{26}Al streaming occurs at un-

usually high velocities and kinematics may be peculiar around regions with a rather young (few Myr) population of massive stars.

Our constraints on large-scale integrated broadening of the ^{26}Al line from the inner Galaxy can be interpreted in terms of interstellar-medium characteristics, if we adopt the contribution of Galactic rotation from a model: For 1 keV broadening due to Galactic rotation (Kretschmer et al. 2003), the intrinsic width from ISM turbulence would be 1.2 keV to obtain our 1σ line width limit of 1.6 keV. This corresponds to 300 km s^{-1} for a 2σ limit on ISM velocities, leaving typical velocities up to $\approx 100 \text{ km s}^{-1}$, well within the acceptable range. Therefore we conclude that, within uncertainties, the average velocities of decaying ^{26}Al in the Galaxy are probably not in excess of typical values for the ISM near massive stars.

Acknowledgements. This paper is based on observations with INTEGRAL, an ESA project with instruments and science data centre funded by ESA member states (especially the PI countries: Denmark, France, Germany, Italy, Switzerland, Spain), Czech Republic and Poland, and with the participation of Russia and the USA. The SPI project has been completed under the responsibility and leadership of CNES/France. The SPI anticoincidence system is supported by the German government through DLR grant 50.0G.9503.0. We are grateful to ASI, CEA, CNES, DLR, ESA, INTA, NASA and OSTC for support.

References

- Chen, W., Gehrels, N., and Diehl R. 1995, ApJ, 444, L57
- Chen, W., Diehl, R., Gehrels, N., *et al.* 1997, ESA-SP, 382, 105
- Cordes, J.M., and Lazio, T.J.W. 2002, astro-ph/0207156
- Diehl, R., Halloin, H., Kretschmer, K., *et al.* 2006, Nature, *in press*
- Diehl, R., Kretschmer, K., Lichti, G.G., *et al.* 2004, ESA-SP, 552, 27
- Diehl, R., Kretschmer, K., Lichti, G.G., *et al.* 2003, A&A, 411, L451
- Diehl, R. 2002, New Ast.Rev., 46, 547.
- Diehl, R., Dupraz, C., Bennett, K., *et al.* 1995, A&A, 298, 445
- Firestone, R.B., Ekström, L.B. 2004, <http://ie.lbl.gov/toi/>
- Gehrels, N., and Chen, W. 1996, A&AS, 120, 331
- Herant, M., and Woosley, S.E. 1994, ApJ, 425, 814
- Jean, P., Vedrenne, G., Roques, J.-P., *et al.* 2003, A&A, 411, L107
- Knödlseeder, J., Valsesia, M., Allain, M., *et al.* 2004, ESA-SP, 552, 33
- Knödlseeder, J., Lonjou, V., Jean, P., *et al.* 2003, A&A, 411, L457
- Knödlseeder, J., Bennett, K., Bloemen, H., *et al.* 1999, A&A, 344, 68
- Knödlseeder, J. 1999, ApJ, 510, 915
- Knödlseeder, J., Dixon, D., Bennett, K., *et al.* 1999, A&A, 345, 813
- Kretschmer, K., Diehl, R., Wang, W., *et al.* 2005, A&A, *in preparation*
- Kretschmer, K., Diehl, R., and Hartmann, D.H. 2003, A&A, 412, L77
- Lin, R.P., Dennis, B.R., Hurford, G.J., *et al.* 2003, Sol.Phys., 210, 3
- Lonjou, V., Knödlseeder, J., Roques, J.-P., *et al.* 2004, ESA-SP, 552, 713
- Mahoney, W. A., Ling, J.C., Jacobson, A.S., and Lingenfelter, R.E. 1982, ApJ, 262, 742
- Mahoney, W.A., Ling, J.C., Wheaton, W.A., and Lingenfelter, R.E. 1984, ApJ, 286, 578
- Metropolis, N., Rosenbluth, A. W., Rosenbluth, M. N., *et al.* 1953, Journ.Chem.Phys., 21, 1087
- Naya, J. E., Barthelmy, S.D., Bartlett, L.M., *et al.* 1996, Nature, 384, 44
- Neal, R. M. 1993, Technical Report CRG-TR-93-1, Dept. of Computer Science, University of Toronto
- Oberlack, U. 1997, Ph. D. Thesis, Technische Universität München
- Oey, M.S. 1996, ApJ, 467, 666
- Plüschke, S., Diehl, R., Schönfelder, V., *et al.* 2001, ESA-SP, 459, 55
- Plüschke, S. 2001, Ph. D. Thesis, Technische Universität München
- Prantzos, N., and Diehl, R. 1996, Phys. Rep., 267, 1, 1
- Robin, A.C., Reylé, C., Derriere, R., Picaud, S. 2003, A&A, 409, 523
- Roques, J.-P., Schanne, S., von Kienlin, A., *et al.* 2003, A&A, 411, L91
- Smith, D. 2004, ESA-SP, 552, 45
- Smith, D. 2003, ApJ, 589, L55
- Strong, A.W., Diehl, R., Halloin, H. *et al.* 2005, A&A, 444, 495
- Strong, A.W., Diehl, R., H. Halloin *et al.* 2004, ESA-SP, 552, 507
- Sturmer, S.J., Shrader, C.R., Weidenspointner, G., *et al.* 2003, A&A, 411, L81
- Sturmer, S. J., and Naya, J. E. 1999, ApJ, 526, 200
- Taylor, J.H., Cordes, J.M. 1993, ApJ, 411, 674
- Vedrenne, G., Roques, J.-P., Schönfelder, V., *et al.* 2003, A&A, 411, L63
- Vink, J.S., and de Koter, A. 2005, A&A, 442, 587
- Weidenspointner, G., Kiener, J., Gros, M., *et al.* 2003, A&A, 411, L113
- Wheelock, S., Chillemi, J., Gautier, N., *et al.* 1991, BAAS, 23, 908
- Winkler, C., Courvoisier, T.C., DiCocco, G., *et al.* 2003, A&A, 411, L1